Catalysis Science & Technology



PAPER View Article Online
View Journal | View Issue



Cite this: Catal. Sci. Technol., 2023, 13, 2360

Propane oxidative dehydrogenation using CO₂ over CrO_x/Fe-CeO₂ catalysts†

Hedun Wang, Thu D. Nguyen and George Tsilomelekis **D**

The kinetic behavior of CrO_x sites supported on Fe doped CeO_2 was studied for CO_2 -assisted propane oxidative dehydrogenation. The support was synthesized via a co-precipitation method of Fe and Ce precursors while wetness impregnation was used to deposit the CrO_x species. XRD and Raman analysis confirmed the presence of dispersed CrO_x sites on the surface of the support at a low loading while small Cr_2O_3 nanoparticles were found at high loadings. The addition of CrO_x sites reconstructs the available surface oxygen sites and enhances the reducibility of the catalyst as confirmed by H_2 -TPR measurements. Herein, we show that the CrO_x based catalysts outperform the parent support at low reaction temperatures both from a propane conversion and propylene selectivity perspective. At elevated temperatures, the effect of CrO_x sites on the propylene production diminishes since propane dry reforming is dominant. A Langmuir–Hinshelwood kinetic model was developed based on 14 elementary steps to account for the dominating reaction pathways, *i.e.* propane dehydrogenation, reverse water gas shift and dry reforming. The regressed kinetic data showed that the incorporation of CrO_x on the support decreases the activation energy of propane dehydrogenation by 60–75% while a small decrease in the activation energy of dry reforming was noted (~15%).

Received 3rd September 2022, Accepted 15th February 2023

DOI: 10.1039/d2cy01563c

rsc.li/catalysis

Introduction

Over the past decade, the US shale gas revolution has played a profound role in the structure of domestic energy and chemical sectors. Recent reports have shown an increase in propane production with the advent of shale gas revolution which in turn directly provides propane at a reduced price as compared to expensive crude oil derivatives. 1-3 The shift to cheap chemical feedstocks offers an incentive for the research community to develop new technologies for propane conversion into value added products. Particularly, 'onpurpose' propylene production has already been successfully applied to industrial manufacturing featuring the Honeywell UOP process.4,5 Although propane conversion via direct dehydrogenation (PDH) is the widely used approach, it suffers from important challenges. The highly endothermic character generally requires vast energy input. In addition, propane conversion is limited due to thermodynamic equilibrium of the PDH reaction, and thus separation and recycling of reactants from a reactor downstream to upstream seems to be crucial to achieve high productivity. Apart from these

potential drawbacks, product separation and catalyst regeneration techniques are essential in order to overcome product selectivity issues due to unavoidable side reactions and coke formation, respectively.⁶

On the other hand, CO2 emission and global warming have become increasingly worse and severe over the past decades. CO2 capture and CO2 conversion related topics have received worldwide attention, with great efforts and achievements from different fields such as photoreduction, 7-9 electroreduction10 and bio-mitigation.11 In the field of propane dehydrogenation to produce propylene, CO2 is also identified as a mild oxidant that can possibly open a more sustainable path with a smaller environmental footprint than dehydrogenation.12 conventional propane thermodynamics and technical barriers make PDH economically challenging, the introduction of CO2 as a soft oxidant provides the following benefits: (1) the overall ODH reaction:

$$C_3H_8 + CO_2 \Rightarrow C_3H_6 + CO + H_2O$$

can be operated under milder conditions than those of direct dehydrogenation reaction; (2) CO_2 -assisted ODH reaction can produce CO and H_2 (syngas) with a suitable ratio, which can be directly incorporated in either downstream F–T synthesis ¹³ or tandem hydroformylation; ¹⁴ (3) coke formation can be suppressed either by reducing the formation of coke

Department of Chemical and Biochemical Engineering, Rutgers University, Piscataway, NJ08854, USA. E-mail: g.tsilo@rutgers.edu

[†] Electronic supplementary information (ESI) available. See DOI: https://doi.org/ 10.1039/d2cy01563c

precursors¹⁵ or by promoting the reverse Boudouard reaction:16,17

$$C(s) + CO_2 \Rightarrow 2CO(g)$$

Despite these benefits, CO2 is considered a "hard-to-activate" molecule due to its unique electronic properties and therefore, seeking catalytic strategies or developing novel materials that involve the activation of both C-H bonds of alkanes and CO2 comprises a formidable challenge.

In our recent work, 18 we have shown that trivalent Fe ions successfully doped into a ceria lattice with a Ce: Fe atomic ratio = 10 (10Fe-CeO2) are a very selective and stable catalyst for the CO2 assisted propane ODH. Building upon our previous efforts, in this work, surface dispersed CrOx species were deposited over our prior stable support, i.e. 10Fe-CeO2, with the intention to study their intrinsic kinetic behavior for CO2-assisted propane dehydrogenation. CrOx species on different types of metal and non-metal oxide supports have been reported in the open literature as promising materials with high catalytic activity towards selective propane dehydrogenation. 19-22 Herein, CrOx/10Fe-CeO2 with different Cr surface densities has been synthesized and evaluated physicochemically, spectroscopically and kinetically to understand its effects on propane dehydrogenation activity and propylene selectivity. A Langmuir-Hinshelwood kinetic model based on experimental results and literature data is also developed to investigate the intrinsic effect of Cr species.

Experimental

Synthesis of catalysts

Ce(NO₃)₃·6H₂O (99.99%), Fe(NO₃)₃·9H₂O (99.95%) and Cr(NO₃)₃·9H₂O (>99.99%) were purchased from Sigma Aldrich and used without further purification. The support, i.e. 10Fe-CeO2, was synthesized via a co-precipitation method of aqueous Fe3+ and Ce3+ species where the entire synthesis is controlled by the crystalline growth mechanism proposed by Wang et al.23 CrO_v/Fe-CeO₂ catalysts were synthesized via incipient wetness impregnation of Cr on calcined 10Fe-CeO2. We denote the catalysts as $nCr/10Fe-CeO_2$, where n is the surface atomic density of Cr. Both 10Fe-CeO2 and nCr/10Fe-CeO2 were calcined at 873 K for 6 hours under an air flow (50 ml min⁻¹).

Catalyst characterization

Raman spectroscopy. Raman spectra were collected with a Horiba Scientific LabRam HR Evolution Raman spectrometer cooled with a Synapse CCD detector (-70 °C). The laser source used (532 nm) was directed on the sample and focused by using a 50× long working distance objective. The power of the laser on the surface of the sample was controlled by using a neutral density filter at low level (5%) to avoid local overheating. In situ Raman experiments were conducted in a Harrick Scientific high-temperature reaction chamber equipped with a SiO2 window. The nominal value of the temperature controller was calibrated with an independent thermocouple that was placed below the catalyst sample.

X-ray powder diffraction. XRD analysis was performed with a PANalytical Philips X'Pert X-ray diffractometer to determine crystallinity and phase composition. The XRD instrument is equipped with a CuKc. source at 45 kV and 40 mA and an angular incidence 2θ between 20° and 90° with 0.05° steps and 4.0 s per step. The phase composition was analysed by whole pattern fitting refinement analysis with a relative error R% targeted below 15%. Silicon was used as an external standard reference to determine any possible peak shift.

Temperature-programmed reduction (H2-TPR)

H2-TPR experiments were conducted to investigate the redox properties of the 10Fe-CeO2 and nCr/10Fe-CeO2 catalysts. In each test, 50 mg sample was loaded into a U-shaped quartz reactor. The sample was pre-treated in air at 600 °C for 1 hour to be fully dehydrated and fully oxidized, after which the sample was isolated in inert gas and cooled down to room temperature. TPR experiments were performed with a 30 sccm flow of 1% H₂/Ar at a ramping rate of 10 °C min⁻¹ from 100 °C to 650 °C and then the temperature was held constant for 20 minutes. The TPR pattern was evaluated by analyzing the water signal (m/z = 18) collected with an in-line mass spectrometer (MKS Cirrus™ 3).

Kinetic experiments. The propane ODH with CO₂ reaction was conducted in a fixed bed quartz tube reactor. 18 Propane (UHP, Praxair), CO2 (UHP, Airgas) and nitrogen (UHP, Airgas) were mixed and co-fed at total flow rates in the range of 20-100 mL min⁻¹ using mass flow controllers (Alicat Scientific). Each catalyst was pre-heated under an oxygen flow up to the desired reaction temperature and isolated in pure nitrogen to ensure no remaining oxygen prior to and inside the reactor. The reactor outflow (product composition) was analysed with a MicroGC (Agilent, 490) equipped with an MS5A column (CH₄, H₂ and CO) and PPQ column (CO₂, C₂H₄, C₂H₆, C₃H₆, C₃H₈ and H₂O). In all kinetic experiments, the catalyst loading (typically 0.1 g catalyst) and total flow rate mass were adjusted to achieve low propane conversion (below 10%). The reaction temperature was varied in the range from 510 to 590 °C. The effect of CO2/C3H8 was also investigated. The propane conversion, product selectivity (on a propane basis) and reaction rates were calculated according to:

$$X_{\rm C_3H_8} = \frac{F_{\rm in,C_3H_8} - F_{\rm out,C_3H_8}}{F_{\rm in,C_3H_8}} \times 100\%$$

$$S_{\rm{C_xH_y}} = \frac{\frac{x}{3} \times F_{\rm{C_xH_y}}}{F_{\rm{in,C_3H_8}} - F_{\rm{out,C_3H_8}}} \times 100\%$$

$$Yield = X_{C_3H_8} \times S_{C_3H_6}$$

$$-r_{\rm C_3H_8} = \frac{{\rm d}F_{\rm C_3H_8}}{{\rm d}w} \cong \frac{X_{\rm C_3H_8}}{w/F_{\rm in,C_3H_8}}$$

$$r_{\rm C_3H_6} = \frac{{
m d}F_{
m C_3H_6}}{{
m d}w} \cong \frac{X_{
m C_3H_8} \times S_{
m C_3H_6}}{w/F_{
m in,C_3H_8}}$$

Results and discussion

Physicochemical characterization and structural implications

Table 1 shows the BET results of the Fe–CeO $_2$ supports and Fe–CeO $_2$ supported CrO $_x$ catalysts (see Fig. S1† for the complete adsorption isotherms). The BET surface area features a monotonic decrease with an increasing amount of Cr loading, which is consistent with supported Cr oxides reported in the literature. $^{20,24-26}$ It is worth noting that n Cr/Fe–CeO $_2$ has a very low pore volume as compared to other materials. 13,20 Small variations in BET measurements in conjunction with plausible surface restructuring on the surface could lead to small fluctuations in the pore volume measurements, as observed in Table 1.

The X-ray diffractograms of $10\text{Fe}-\text{CeO}_2$ and $n\text{Cr}/10\text{Fe}-\text{CeO}_2$ with various Cr loadings shown in Fig. 1 did not present any bulk crystalline oxide phases relevant to hematite and/or Cr_2O_3 , suggesting that the support maintained its crystalline form while ensuring good Cr distribution. Below the monolayer coverage, the impregnation of Cr species on $10\text{Fe}-\text{CeO}_2$ will result in the anchoring of amorphous surface species, usually acknowledged as a tetrahedral $\text{Cr}(v_1)\text{O}_4$ structure under fully oxidized and fully dehydrated conditions. Depending on the surface density of Cr species, the unit structure can either remain as isolated monochromate or agglomerate to form polychromate species via Cr-O-Cr bonds.

In Fig. 2a, we report the *in situ* Raman spectra of all the $n\text{Cr}/10\text{Fe-CeO}_2$ catalysts under fully oxidized and dehydrated conditions at 550 °C. The most intense peak centred at \sim 450 cm⁻¹ corresponds to the F_{2g} vibrational mode of the ceria support. The observed red shift of approximately 15 cm⁻¹ from the pure CeO₂ (usually observed at 465 cm⁻¹) is related to the incorporation of Fe dopants inside the ceria lattice $^{30-32}$ and depends on the Fe/Ce atomic ratio. The broad feature that appears at 590 cm⁻¹ is assigned as an oxygen defect-related band and the ratio of peak intensity I_{590}/I_{450} has been regarded as an indirect indicator of the relative abundance of oxygen vacancies 33,34 in CeO₂. Upon

Table 1 Summary of BET results of Cr/Fe-CeO₂ catalysts

Catalyst	$^{\rm BET}_{\left(m^2\;g^{-1}\right)}$	Pore width (nm)	Pore volume (cm³ g ⁻¹)
10Fe-CeO ₂	62	20	0.41
1Cr/10Fe-CeO ₂	57	23	0.34
2Cr/10Fe-CeO ₂	52	32	0.41
4Cr/10Fe-CeO ₂	42	33	0.33

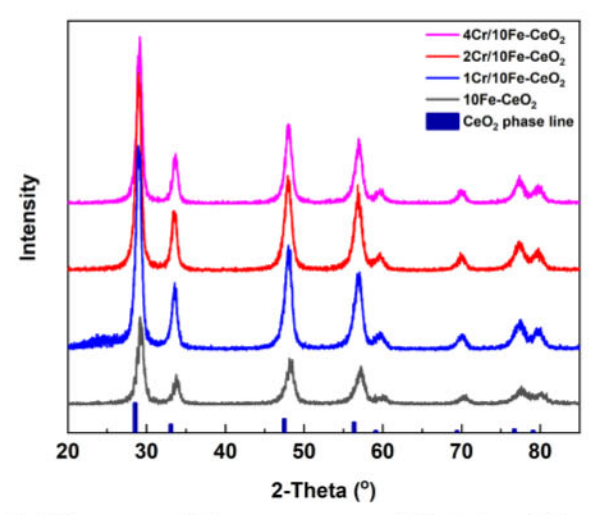


Fig. 1 XRD patterns of the parent support, 10Fe-CeO_2 and the $n\text{Cr}/10\text{Fe-CeO}_2$ catalysts with various Cr loadings.

impregnation of chromium species, new peaks evolved at 539 cm⁻¹, 837 cm⁻¹, 998 cm⁻¹ and 1026 cm⁻¹. The peaks at 998 cm⁻¹ and 1026 cm⁻¹ were assigned to isolated and polymeric Cr=O vibration, respectively. 20,35,36 The broad band located at around 837 cm⁻¹ is associated with either the symmetric stretching of O-Cr-O (ref. 37 and 38) or Cr-O-Cr (ref. 39) (845 cm⁻¹) structures; however, there is a consensus that this peak is associated with the presence of polymeric species. Our Raman results are consistent with this assignment since the integrated area under the 840 cm⁻¹ peak increases with increasing Cr loading. Besides, a sharp peak at 539 cm⁻¹ over the 4Cr/10Fe-CeO2 oxide pertains to the A1g symmetric vibrational mode of Cr2O3.39 In addition, the normalized peak intensity for the F2g vibration decreases significantly over the 4Cr/10Fe-CeO2 oxide. Even though the XRD data revealed no crystalline phases of chromium oxide, the Raman

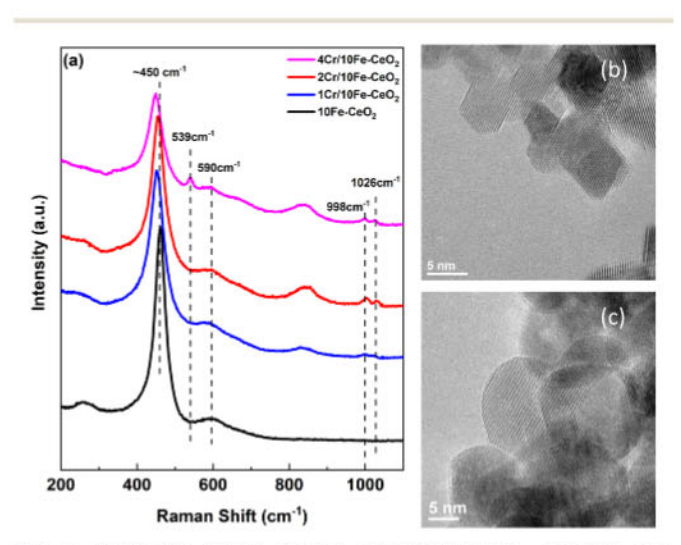


Fig. 2 (a) In situ Raman spectra of $Cr-10Fe-CeO_2$ catalysts with different Cr loadings under fully oxidized and dehydrated conditions. (b) TEM image of the $10Fe-CeO_2$ sample. (c) TEM image of $2Cr/10Fe-CeO_2$ oxide.

results suggest the formation of chromium crystalline phases (nano-sized) at a high Cr surface density (i.e. 4Cr per nm²) indicating the overreaching of monolayer coverage on the surface. Relevant 10Fe-CeO₂ oxide TEM (Fig. 2b and c) show changes in the textural properties after impregnation of Cr oxides. While the original Fe-CeO2 exhibits a well-defined hexagonal shape, the addition of Cr oxides modified the external surface turning into sphericallike agglomerates.

Reducibility and active surface oxygen sites

H2-TPR experiments were conducted to reveal the difference in the redox properties of the catalysts due to the change of the available surface oxygen species with different bonding and electronic environments. All TPR experiments were performed up to a maximum temperature of 650 °C to ensure that the mesoporous structure of the support will remain while avoiding the potential phase separation of cerianite and hematite.18 In Fig. 3a, the H2-TPR data for the representative catalysts and pure CeO2 (for comparison) are presented. Bare CeO2 shows a broad peak centred at 550 to 600 °C, which is attributed to the reduction of reactive surface oxygen species. 40,41 Since the total reduction of CeO2 to Ce₂O₃ is only expected in the temperature range of 800 to 900 °C, the broad reduction band suggests the creation of oxygen defects and exposure of Ce3+ on the surface. 40,42,43 This argument is also supported by our in situ Raman H2-TPR results in Fig. 3b and c. The band at 245 cm⁻¹, representing the transverse acoustic mode of surface oxygen,44 is gradually decreased during H2-TPR. In addition, we observe an increase in the relative peak intensity ratio (~590 cm⁻¹/450 cm⁻¹), which indicates an increase in the defect domains (oxygen vacancies).28 Upon doping of Fe into the cerium oxide lattice, the main peak shifted to around 360

°C, indicating the enhanced surface reducibility as compared to bare CeO2. 45,46 Despite the presence of Fe ions in the bulk phase, the early TPR-H2 feature is not due to the reduction of crystalline Fe2O3 since all relevant characterization results, i.e., XRD and Raman, as well as prior extensive characterization of our support,18 confirm the absence of a separated crystalline iron oxide phase. Thus, the feature at around 360 °C should be attributed to the weakening of the lattice bonds between metal ions and O due to heteroatom doping which is strongly supported by the shift in the diffractogram. As stated in our previous work,18 the surface oxygen to Fe-CeO2 oxide should be predominately involved in two types of structures: Fe-rich sites (Fe-O-Ce) and Fe-free sites (Ce-O-Ce). A new peak appeared at around 470 °C, which has been previously assigned as adsorbed peroxide (O_2^{2-}) or superoxide (O_2^{-}) species on oxygen vacancies²⁸ due to long-time calcination. However, we cannot exclude the possibility that the addition of Fe ions into the CeO2 lattice structure may also weaken the bond strength of metal-O leading to an increase in the apparent reducibility of oxygen species at the surface. The impregnation of CrOx sites reconstructs the surface through the formation of a Cr-Osupport bridging bond in order to balance its degree of coordinative unsaturation,47 during which the original surface oxygen sites may be consumed or diffuse into subatomic layers. As a result, those oxygen sites are no longer exposed or accessible to H2 in the gas phase. 48 Particularly, at high Cr loadings approaching monolayer coverage (2Cr/ 10Fe-CeO2 and 4Cr/10Fe-CeO2) when polymeric CrOx species dominate the catalyst surface, we observe a decrease in the total area of H2 consumed. The original Fe-rich sites disappeared from the TPR signals and a broad band starting from ~400 °C and centred at ~500 °C indicates the formation of new oxidation sites. Interestingly, the Raman data revealed that the band at around 845 cm⁻¹ disappeared

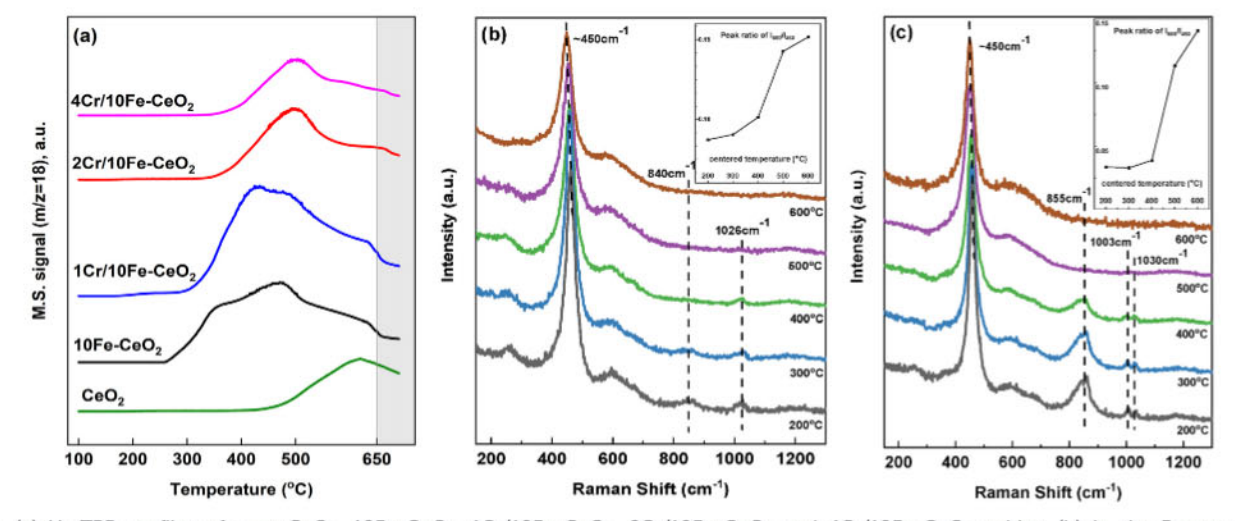


Fig. 3 (a) H₂-TPR profiles of pure CeO₂, 10Fe-CeO₂, 1Cr/10Fe-CeO₂, 2Cr/10Fe-CeO₂ and 4Cr/10Fe-CeO₂ oxides, (b) in situ Raman spectra coupled with H2-TPR experiments of 1Cr/10Fe CeO2. (c) In situ Raman spectra coupled with H2-TPR experiments of 2Cr/10Fe-CeO2. Insert: Peak ratios I₅₉₀/I₄₅₀ of 1Cr/10Fe-CeO₂ and 2Cr/10Fe-CeO₂ during H₂-TPR at different temperature stages.

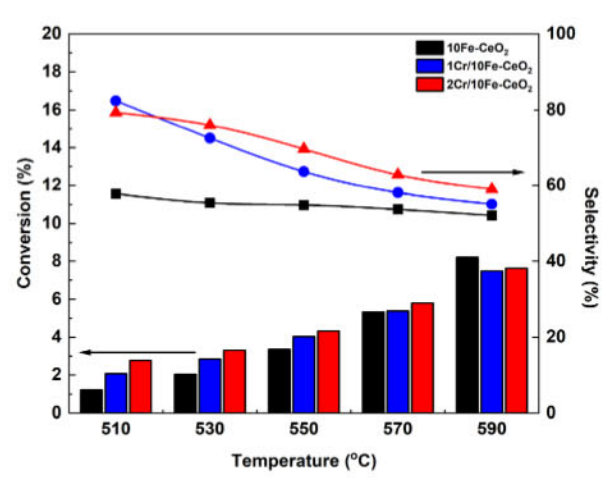


Fig. 4 Catalytic performance of 10Fe–CeO₂ and Cr supported 10Fe–CeO₂ catalysts under an intrinsic kinetic regime. Exp. parameters: 510 to 590 °C, 1 atm, 100 mL min⁻¹ total flow with 5% propane and 5% carbon dioxide, 100 mg catalyst loading.

prior to that at $\sim 1000-1030~{\rm cm}^{-1}$ pointing that the broad feature at around 430 °C corresponds to the Cr–O bridging bonds while that at $\sim 500~{\rm °C}$ corresponds to the Cr–O terminal bonds.

Kinetic studies

Effect of temperature. The effect of temperature on the performance of all the catalysts was evaluated in the 510-590 °C range. The total flow and mass of the catalyst were appropriately selected to ensure that all measurements were performed at the kinetic regime. Fig. 4 shows the temperature dependent propane conversion and propylene selectivity for 10Fe-CeO2, 1Cr/10Fe-CeO2 and 2Cr/10Fe-CeO2. The overall behaviour is consistent with an improved catalytic performance (propylene yield) upon addition of chromium sites on the surface of 10Fe-CeO2. The propylene selectivity decreases with increasing temperature for the Crbased catalysts while, interestingly, it remains almost constant for the bare support. This behaviour is indicative of the supported CrO_x sites providing unique surface properties that unlock selective dehydrogenation pathways which are kinetically more favourable at low temperatures. This is also consistent with the H2-TPR and Raman measurements discussed above where the presence of Cr-O and Cr=O can be regarded as surface oxygen sites for propane adsorption. However, after dehydrogenation, oxygen defects/vacancies have to be replenished by CO2. Thus, next we evaluate the effect of CO2 on the intrinsic kinetics.

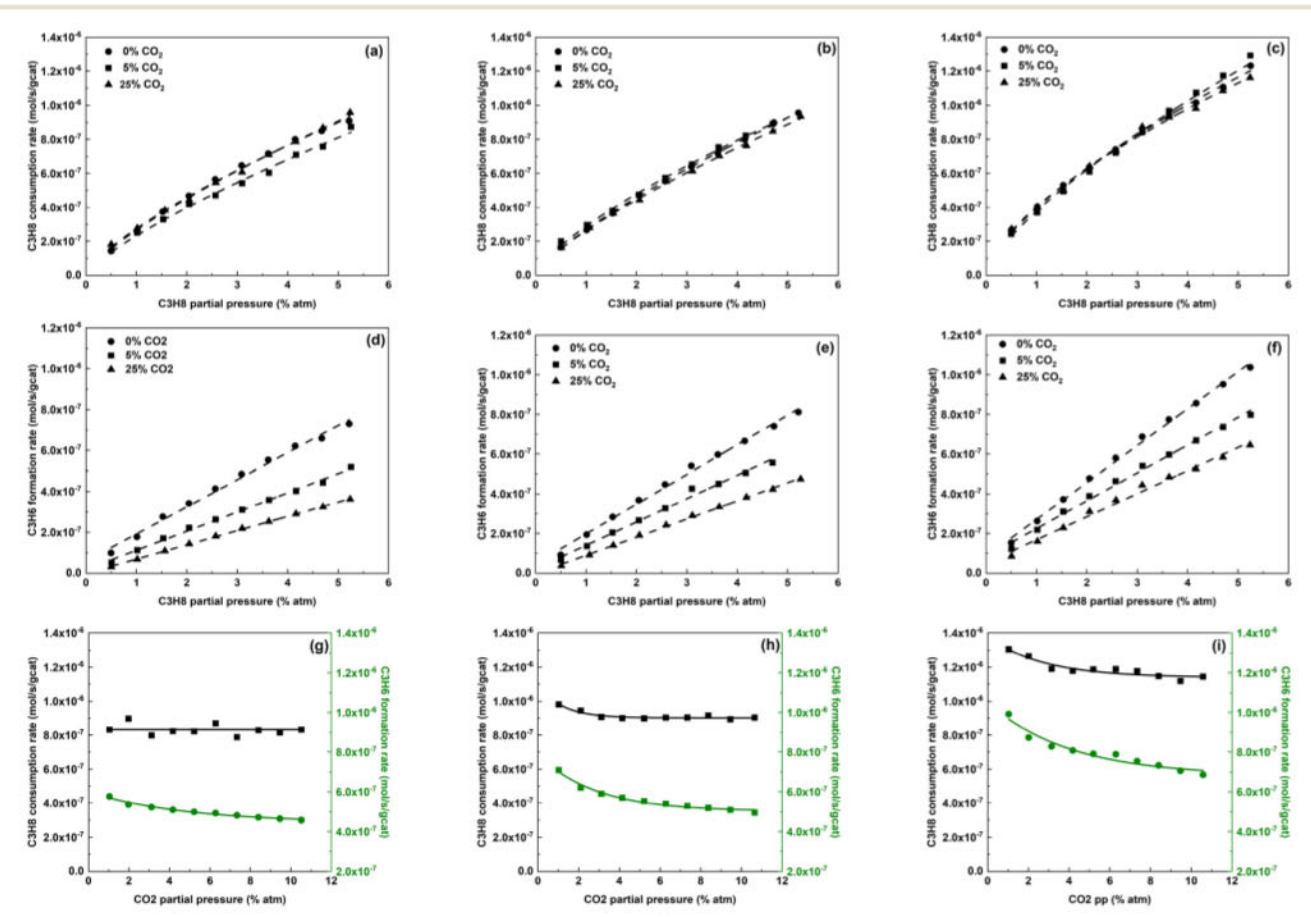


Fig. 5 Kinetic behaviour of the 10Fe–CeO₂ (a, d and g), 1Cr/10Fe–CeO₂ (b, e and h) and 2Cr/10Fe–CeO₂ (c, f and i) catalysts with respect to changes in the partial pressure of propane and CO₂. Reactivity is investigated at 550 °C. (a–c) Propane consumption rate, (d–f) propylene formation rate, and (g–i) propane and propylene reaction rates as a function of CO₂ partial pressure.

Effect of reactant partial pressure on rates. The effects of partial pressure and the ratio of propane to CO2 on reactivity were studied at 550 °C under differential conditions. Relevant results are summarized in Fig. 5. Upon increasing CO2, the rate of propane consumption appears to be unaffected (Fig. 5a-c) underscoring that CO2 is not involved in the rate controlling step of propane activation, especially under low partial pressure conditions where competitive adsorption will not play a significant role. In the case of the bare support (Fig. 5g), the rate of propane consumption remains constant upon increasing the partial pressure of CO2 in the reaction stream, while for the CrOx based catalysts, propane consumption slightly decreased with a small increase of CO2 and then remained constant (Fig. 5h and i). On the other hand, the rate of propylene formation decreases monotonically (Fig. 5d-f) with increasing CO2. This decrease is ascribed to a shift from direct dehydrogenation to the thermodynamically favorable dry reforming under high CO2/C3H8 conditions; the higher the CO2 in the feed, the larger the dry reforming (DRF) contribution. In general, the addition of chromium species increases both the intrinsic rates of propane consumption and propylene formation highlighting the positive impact of CrOx on productivity. The beneficial effect of CO2 on the propylene formation has been underscored in the literature. 49,50 However, it is worth mentioning that the effect of CO2 on the overall propane conversion and propylene formation depends on multiple factors that may include the nature of active sites present which in turn may govern the relative contribution of simultaneous reactions such as DH vs. reforming⁵¹ and/or DH/ ODH.52 Moreover, CO2 may participate directly in reoxidizing reduced metal oxide centers; thus, its conversion competes with the reverse water gas shift reaction.

The rate of propane consumption can be represented by the following power-law kinetic expression:

$$-r_{\mathrm{C_3H_8}} = k_{\mathrm{app}} P_{\mathrm{C_3H_8}}^{\alpha} P_{\mathrm{CO_2}}^{\beta},$$

where α and β are the apparent reaction orders for propane and CO2, respectively. Numerical values of the apparent orders for propane conversion are given in Table 2 and the relevant analysis is in Fig. S4.† It is shown that the apparent propane reaction order for 10Fe-CeO2, 1Cr/10Fe-CeO2 and 2Cr/10Fe-CeO₂ is 0.71, 0.74 and 0.64, respectively. The actual apparent order is expected between 1 and 0.33 depending on the relative contribution of PDH and DRF. The values reported in this study are in agreement with a recent kinetic study by Shishido et al. 53 where the reaction orders of partial pressure of propane over Cr/SiO2 and Cr/Al2O3 catalysts were found to be

Table 2 Summary of the apparent reaction orders of propane consumption rate and propane overall activation energy

Catalyst	C_3H_8 reaction order (α)	CO_2 reaction order (β)		
10Fe-CeO ₂	0.71	-0.06		
1Cr/10Fe-CeO2	0.74	-0.03		
2Cr/10Fe-CeO ₂	0.64	-0.02		

0.65 and 0.59, respectively. It is also shown that propane conversion has an almost zeroth order dependence on CO2. The kinetic data of this study were collected at a low partial pressure regime (from 0.5% to 5%), where competitive adsorption of propane and CO2 may not be taken into account. According to Chen et al.,51 competitive adsorption and reduction of C3H8 reaction rates occur severely when CO2 in the feed exceeds a certain partial pressure threshold depending on the type of active sites and support surface.

Mechanistic implications and the Langmuir-Hinshelwood model

The characterization and kinetic results discussed in the previous sections set the foundation to propose the following steady-state kinetic model that assumes: (a) two types of (identified from previous literature reports 18,45,54,55), i.e. surface active oxygen sites (S1) and oxygen vacancies (S2); (b) no migrations of adsorbed intermediates between S1 and S2 sites; (c) single site adsorption; (d) the Langmuir-Hinshelwood-Hougen-Watson (LHHW) surface reaction mechanism was applied to describe the overall reaction network comprising PDH, DRF and RWGS assuming a primary rate-limiting step (p-rds) and two secondary rate-limiting steps (s-rds). Based on these assumptions, the kinetics observed in this work can be rationalized using the following 14 elementary steps:

$$\begin{split} s1: & \operatorname{C_3H_8}(g) + 2S_1 \ \rightleftharpoons \ \operatorname{C_3H_7_S_1} + \operatorname{H_S_1} \\ \\ s2: & \operatorname{C_3H_7_S_1} \ \rightleftharpoons \ \operatorname{C_3H_6}(g) + \operatorname{H_S_1} \\ \\ s3: & \operatorname{2H_S_1} \ \rightleftharpoons \ \operatorname{H_2}(g) + 2S_1 \\ \\ s4: & \operatorname{CO_2}(g) + S_2 \ \rightleftharpoons \ \operatorname{CO}(g) + S_1 \\ \\ s5: & \operatorname{CO_2}(g) + S_2 + \operatorname{H_S_1} \ \rightleftharpoons \ \operatorname{COOH_S_2} + S_1 \\ \\ s6: & \operatorname{COOH_S_2} \ \rightleftharpoons \ \operatorname{CO}(g) + \operatorname{HO_S_2} \\ \\ s7: & \operatorname{2HO_S_2} \ \rightleftharpoons \ \operatorname{H_2O}(g) + S_1 + S_2 \\ \\ s8: & \operatorname{C_3H_7_S_1} + S_1 \ \rightleftharpoons \ \operatorname{CH_3CH_S_1} + \operatorname{CH_3_S_1} \\ \\ s9: & \operatorname{CH_3CH_S_1} + S_1 \ \rightleftharpoons \ \operatorname{CH_3_S_1} + \operatorname{CH_S_1} \\ \end{split}$$

s10: $CH_3_S_1 \rightleftharpoons CH_3O_S_2$

s11:
$$CH_S_1 \rightleftharpoons CHO_S_2$$

$$s12: CH_3O_S_2 + S_1 \Rightarrow CH_2O_S_2 + H_S_1$$

s13:
$$CH_2O_S_2 + S_1 \Rightarrow CHO_S_2 + H_S_1$$

$$s14: CHO_S_2 + S_1 \Rightarrow CO(g) + H_S_1 + S_2$$

In this proposed reaction scheme, the reactant molecules, C3H8 and CO2, are independently adsorbed and activated on surface oxygen sites and oxygen vacancies, respectively. The formed C3H7-S1 is hypothesized to further evolve via two distinct reaction paths: i) secondary dehydrogenation resulting in the desired olefin via PDH and/or ii) C-C scissoring. For the latter case, the light hydrocarbon species can further react through two competitive paths where i) upon the participation of oxygen sites, it will lead to dry reforming products or ii) it will produce coke precursors which migrate to form coke and block certain active sites. It has been suggested that small hydrocarbon species may further decompose into atomic carbon and then oxidized to form CO.56,57 Recently, however, by means of computational efforts, it was shown that low hydrocarbon species (CHx) can be involved in a surface elementary reaction with O* or -OH to form CH_xO.⁵⁸⁻⁶⁰ In this work, the latter is considered more realistic since the Fe-CeO2

they completely turned into atomic carbon. ¹⁸ In addition, our previous work showed minimum coke formation over the 10Fe-CeO₂ surface, which further reduces the possibility of atomic carbon formation, especially at low propane conversion. On the other hand, CO₂ is adsorbed independently on the surface. The activation of CO₂ is fulfilled *via* two possible approaches: direct dissociation to generate adsorbed CO and O* (ref. 18, 55, 61 and 62) or combination with adsorbed hydrogen atoms (mostly generated *via* the propane C-H activation step) and formation of carboxyl intermediates (-COOH), which further decompose to CO and hydroxyl groups (-OH). The latter is also known as the associative mechanism of the reverse water–gas shift reaction.

Assuming s14 as the primary rate-limiting step and s1 and s4 as the secondary rate-limiting steps, the overall PDH, DRF and RWGS rates are expressed as:

$$r_{\rm DH} = \frac{k_{\rm DH} \left(P_{\rm C_3H_8} P_{\rm H_2}^{-1/2} - \frac{P_{\rm C_3H_6} P_{\rm H_2}^{-1/2}}{\kappa_{\rm DH}} \right)}{\left[1 + K_2^{-1} P_{\rm C_3H_6} (K_{\rm H_2} P_{\rm H_2})^{0.5} + (K_{\rm H_2} P_{\rm H_2})^{0.5} \right]}$$

$$r_{\rm RWGS} = \frac{k_{\rm RWGS} \bigg(P_{\rm CO_2}^{~2} P_{\rm CO}^{~2} P_{\rm H_2} - \frac{P_{\rm H_2O}}{K_{\rm RWGS}} \bigg)}{\bigg(1 + K_5 P_{\rm CO_2} \big(K_{\rm H_2} P_{\rm H_2} \big)^{0.5} \bigg(1 + \frac{K_5}{P_{\rm CO}} \bigg) + \frac{K_{\rm CHO} P_{\rm C_3 H_6}^{~1/3} P_{\rm CO_2}}{P_{\rm CO} \big(P_{\rm H_2} \big)^{\frac{1}{2}}} \bigg)^2}$$

$$r_{\mathrm{DRF}} = \frac{k_{\mathrm{DRF}} \Bigg[P_{\mathrm{C_{3}H_{8}}}^{1/3} P_{\mathrm{CO_{2}}} P_{\mathrm{CO}}^{-1} P_{\mathrm{H_{2}}}^{-5/6} - \frac{P_{\mathrm{CO}} P_{\mathrm{H_{2}}}^{1/2}}{K_{\mathrm{DRF}}} \Bigg] \Big[1 + K_{2}^{-1} P_{\mathrm{C_{3}H_{6}}} (K_{\mathrm{H_{2}}} P_{\mathrm{H_{2}}})^{0.5} + (K_{\mathrm{H_{2}}} P_{\mathrm{H_{2}}})^{0.5} \Big]^{-1}}{1 + K_{5} P_{\mathrm{CO_{2}}} (K_{\mathrm{H_{2}}} P_{\mathrm{H_{2}}})^{0.5} \Bigg(1 + \frac{K_{5}}{P_{\mathrm{CO}}} \Bigg) + \frac{K_{\mathrm{CHO}} P_{\mathrm{C_{3}H_{6}}}^{1/3} P_{\mathrm{CO_{2}}}}{P_{\mathrm{co}} (P_{\mathrm{H_{2}}})^{\frac{1}{2}}}$$

oxides were shown to have reactive surface oxygen sites that could readily oxidize low hydrocarbon intermediates before Details of the regressed kinetic parameters are summarized in Table 3 and a parity plot of the predicted rates with respect

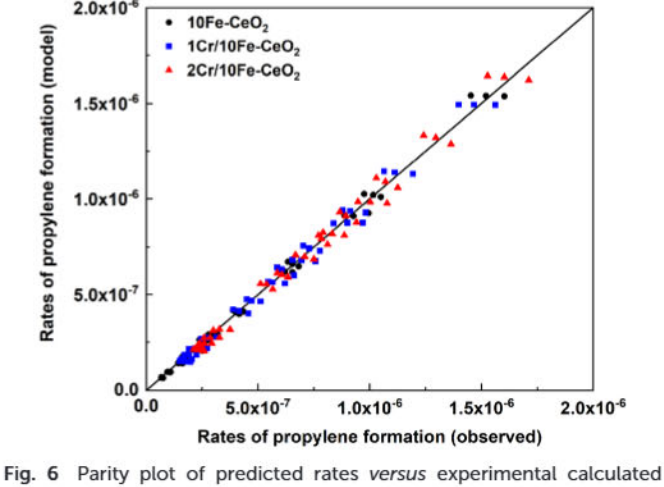
Table 3 Summary of reaction rate constants and reactants' adsorption equilibrium constants regressed by the steady-state model and activation energies reported in the literature obtained by experimental and computational studies

Catalyst (this work)	PDH		DRF	
	k ₀ (at 550 °C)	$E_{\rm a}$ (kJ mol ⁻¹)	k ₀ (at 550 °C)	E_a (kJ mol ⁻¹)
10Fe-CeO ₂	$1.49 \times 10^{-5} (\pm 9.6 \times 10^{-7})$	109 (±2.4)	$2.57 \times 10^{-5} (\pm 9.4 \times 10^{-6})$	
1Cr/10Fe-CeO ₂	$1.97 \times 10^{-5} (\pm 1.5 \times 10^{-6})$	44.4 (±7.1)	$3.6 \times 10^{-5} (\pm 1.3 \times 10^{-6})$	140 (±8.4)
2Cr/10Fe-CeO ₂	$2.68 \times 10^{-5} (\pm 2.4 \times 10^{-6})$	28.4 (±4.1)	$4.15 \times 10^{-5} (\pm 1.5 \times 10^{-6})$	120 (±11)
	62563654-0217-084555		and delegant specific and the specific	115 (±17)

Catalyst	PDH, $E_{\rm a}$ (kJ me	ol^{-1})	Catalyst	DRF, $E_{\rm a}$ (kJ mol ⁻¹)
Pt-Sn/CeO ₂ (ref. 66)	41.5	DFT	Co ₃ Pt ₁ /CeO ₂ (ref. 67)	126	Arrhenius plot
Cr/Al ₂ O ₃ (ref. 68)	35.5	Model regression	Co-Ni/Al ₂ O ₃ (ref. 69)	92.3	Arrhenius plot
NbO_x/CeO_2 (ref. 70)	45.2-69.2	Arrhenius plot	Ni ₃ Pt/CeO ₂ (ref. 51)	119	DFT
$Cr/SiAlO_x$ (ref. 71)	Up to 40	Enthalpy of activation	Ni/Mg(Al)O (ref. 72)	93	Arrhenius plot

Literature reported activation energies for propane direct dehydrogenation (PDH) and dry reforming (DRF) for different catalytic systems and methods used.

Sublished on 16 February 2023. Downloaded by Rutgers University Libraries on 1/31/2024 6:25:43 PM.



rates.

to the observed rates for 10Fe-CeO2, 1Cr/10Fe-CeO2 and 2Cr/ 10Fe-CeO2 is also shown in Fig. 6. Activation energies of propane dehydrogenation and dry reforming over similar reported catalyst systems are summarized in Table 3 for comparison. In Fig. S2,† we show data for the propane conversion vs. W/F. We show that at low flow rates, i.e., below 50 ml min⁻¹, some deviation from linear behavior is observed which may point to small transport limitations. It is worth mentioning here that all the data that have been used for the kinetic analysis and regression pertain to a flow rate of 100 ml min⁻¹, thus ensuring no transport limitations. As seen from Table 3, the activation energy for CO2-assisted propane dehydrogenation is 109 kJ mol⁻¹ for the bare support. Upon impregnating Cr on the Fe-CeO2 surface, the activation energy was decreased drastically down to 44.4 and 28.4 kJ mol⁻¹, depending on the Cr surface density. The differences in activation energy implies that as compared to the bare support surface, propane molecules are preferably activated on the Cr active sites. On the other hand, the activation energies of propane dry reforming are less affected by supported Cr species, indicating that the dry reforming pathway is mostly due to the Fe-CeO2 oxide support. CrOx active sites are more selective towards dehydrogenation, which is also consistent with high selectivity reported in most Cr-related catalysts (Cr/ silica, 20,25,73 Cr/SBA, 74,75 Cr/Al₂O₃, 75 etc.) in CO₂-assisted propane dehydrogenation.

Fig. 6 compares the results of the kinetic model with all the catalytic data reported previously for the rate of propylene formation. The model predictions for the propane consumption are also reported in Fig. S5 in the ESI.† The proposed model in this work predicts well both propane consumption and propylene production rates. It should be noted though that the developed kinetic model should be used for predicting the catalytic behavior solely within the reaction conditions of this study and especially at low to moderate CO2 partial pressure. As stated previously, competitive adsorption of propane and CO2 needs to be

considered at a high partial pressure regime (above 15%), which may significantly alter the adsorption constants of both propane and CO₂. Besides, at elevated temperatures, e.g. approaching 800 °C, the net rate of C-C cracking and coke formation⁷⁶ will be boosted and lead to a deficiency in the

total carbon and hydrogen balance. In this case, an additional deactivation model will be required in the future to better describe the extended reaction network.

Conclusions

nCr/10Fe-CeO2 catalysts with different Cr loadings were synthesized via a two-step approach. Raman spectroscopy was utilized to investigate the molecular structure of the surface species confirming the presence of monomeric and polymeric CrO_x sites. The CO₂-assissted propane dehydrogenation reaction was performed over the bare 10Fe-CeO2 support and all the supported chromium catalysts. Our catalytic data in the intrinsic kinetic regime revealed that the Cr-supported catalysts provided improved initial propane conversion and propylene selectivity at low temperatures. Combining the data from H2-TPR, Raman spectroscopy and kinetic analysis together with the proposed model, we show that although DH will be promoted due to CrOx addition, the enhanced reducibility of such sites leads to an apparent increase of the DRF pathway at high temperatures. The overall consumption rate of propane was mainly dependent on the partial pressure of propane with an apparent reaction order of ~0.7, whereas the CO2 partial pressure significantly hampered the overall propylene selectivity. A steady-state kinetic model was developed to account for the major reaction pathways, which are PDH, DRF and RWGS, occurring simultaneously at the temperature range of this work. Reaction rate constants and reactants' adsorption constants were regressed from kinetic data, from which it was observed that the addition of CrO_x decreases the activation energy of PDH by 60-75% as compared to the bare support; the effect of CrOx on the activation energy of DRF was much smaller.

Conflicts of interest

There are no conflicts to declare.

Acknowledgements

This material is based upon work supported in part by Rutgers, The State University of New Jersey, and the National Science Foundation Award #1751683. The authors would like to thank Prof. T. Asefa for helping with the BET measurements and porosity analysis, Prof. W. Zheng from the University of Delaware for TEM analysis and discussion, and Prof. F. Celik for discussion in kinetic analysis.

References

1 E. E. Stangland, Annu. Rev. Chem. Biomol. Eng., 2018, 9, 341-364.

- 2 Y. Chen and J. Xu, J. Cleaner Prod., 2019, 229, 399-411.
- 3 K. Aruga, J. Unconv. Oil Gas Resour., 2016, 14, 1-5.
- 4 S. Chen, X. Chang, G. Sun, T. Zhang, Y. Xu, Y. Wang, C. Pei and J. Gong, *Chem. Soc. Rev.*, 2021, 50, 3315–3354.
- 5 S. Dong, N. R. Altvater, L. O. Mark and I. Hermans, *Appl. Catal.*, A, 2021, 617, 118121.
- 6 F. Cavani, N. Ballarini and A. Cericola, *Catal. Today*, 2007, 127, 113–131.
- 7 S. Gong, G. Zhu, R. Wang, F. Rao, X. Shi, J. Gao, Y. Huang, C. He and M. Hojamberdiev, *Appl. Catal.*, B, 2021, 297, 120413.
- 8 S. Mazzanti, S. Cao, K. ten Brummelhuis, A. Völkel, J. Khamrai, D. I. Sharapa, S. Youk, T. Heil, N. V. Tarakina, V. Strauss, I. Ghosh, B. König, M. Oschatz, M. Antonietti and A. Savateev, *Appl. Catal.*, B, 2021, 285, 119773.
- 9 Y. Liu, C. Miao, P. Yang, Y. He, J. Feng and D. Li, Appl. Catal., B, 2019, 244, 919–930.
- 10 P. Lu, Y. Yang, J. Yao, M. Wang, S. Dipazir, M. Yuan, J. Zhang, X. Wang, Z. Xie and G. Zhang, *Appl. Catal.*, B, 2019, 241, 113–119.
- 11 P. C. Sahoo, R. Kumar, M. Kumar, S. Kumar Puri and S. S. V. Ramakumar, Int. J. Greenhouse Gas Control, 2019, 90, 102785.
- 12 M. A. Atanga, F. Rezaei, A. Jawad, M. Fitch and A. A. Rownaghi, *Appl. Catal.*, B, 2018, 220, 429–445.
- 13 P. Michorczyk, P. Pietrzyk and J. Ogonowski, Microporous Mesoporous Mater., 2012, 161, 56–66.
- 14 Z. H. Xie, H. Y. Guo, E. R. Huang, Z. T. Mao, X. B. Chen, P. Liu and J. G. Chen, ACS Catal., 2022, 12(14), 8279–8290.
- F. Solymosi, P. Tolmacsov and K. Kedves, J. Catal., 2003, 216, 377–385.
- 16 B. Xu, B. Zheng, W. Hua, Y. Yue and Z. Gao, J. Catal., 2006, 239, 470–477.
- 17 B. Xu, B. Zheng, W. Hua, Y. Yue and Z. Gao, Stud. Surf. Sci. Catal., 2007, 170, 1072–1079.
- 18 H. Wang and G. Tsilomelekis, Catal. Sci. Technol., 2020, 10, 4362–4372.
- 19 K. Takehira, Y. Ohishi, T. Shishido, T. Kawabata, K. Takaki, Q. Zhang and Y. Wang, J. Catal., 2004, 224, 404–416.
- 20 J. Baek, H. J. Yun, D. Yun, Y. Choi and J. Yi, ACS Catal., 2012, 2, 1893–1903.
- 21 J. F. S. de Oliveira, D. P. Volanti, J. M. C. Bueno and A. P. Ferreira, *Appl. Catal.*, A, 2018, 558, 55–66.
- 22 X. Zhang, Y. Yue and Z. Gao, Catal. Lett., 2002, 83, 19-25.
- 23 Z. Wang, Y. Xin, Z. Zhang, Q. Li, Y. Zhang and L. Zhou, Chem. Eng. J., 2011, 178, 436–442.
- 24 P. Kuśtrowski, P. Michorczyk, L. Chmielarz, Z. Piwowarska, B. Dudek, J. Ogonowski and R. Dziembaj, *Thermochim. Acta*, 2008, 471, 26–32.
- 25 D. Yun, J. Baek, Y. Choi, W. Kim, H. J. Lee and J. Yi, ChemCatChem, 2012, 4, 1952–1959.
- 26 M. A. Botavina, Y. A. Agafonov, N. A. Gaidai, E. Groppo, V. Cortés Corberán, A. L. Lapidus and G. Martra, *Catal. Sci. Technol.*, 2016, 6, 840–850.
- 27 M. Cherian, M. S. Rao, A. M. Hirt, I. E. Wachs and G. Deo, J. Catal., 2002, 211, 482–495.

- 28 Z. Wu, A. J. Rondinone, I. N. Ivanov and S. H. Overbury, J. Phys. Chem. C, 2011, 115, 25368–25378.
- 29 B. Penkala, D. Aubert, H. Kaper, C. Tardivat, K. Conder and W. Paulus, Catal. Sci. Technol., 2015, 5, 4839–4848.
- 30 S. Chong, G. Zhang, N. Zhang, Y. Liu, J. Zhu, J. Huang and S. Fang, *Ultrason. Sonochem.*, 2016, 32, 231–240.
- 31 K. Li, M. Haneda, P. Ning, H. Wang and M. Ozawa, Appl. Surf. Sci., 2014, 289, 378–383.
- 32 O. H. Laguna, M. A. Centeno, M. Boutonnet and J. A. Odriozola, *Appl. Catal.*, B, 2011, 106, 621–629.
- 33 M.-F. Luo, Z.-L. Yan, L.-Y. Jin and M. He, J. Phys. Chem. B, 2006, 110, 13068–13071.
- 34 M. Ridwan, R. Tamarany, J. Han, S. W. Nam, H. C. Ham, J. Y. Kim, S. H. Choi, S. C. Jang and C. W. Yoon, RSC Adv., 2015, 5, 89478–89481.
- 35 E. L. Lee and I. E. Wachs, J. Phys. Chem. C, 2007, 111, 14410–14425.
- 36 S. D. Yim and I.-S. Nam, J. Catal., 2004, 221, 601-611.
- 37 T. A. Bugrova, V. V. Dutov, V. A. Svetlichnyi, V. Cortés Corberán and G. V. Mamontov, *Catal. Today*, 2019, 333, 71–80.
- 38 D. S. Kim and I. E. Wachs, J. Catal., 1993, 142, 166-171.
- 39 H. Xie, H. Wang, Q. Geng, Z. Xing, W. Wang, J. Chen, L. Ji, L. Chang, Z. Wang and J. Mao, *Inorg. Chem.*, 2019, 58, 5423-5427.
- 40 Z. Zhang, D. Han, S. Wei and Y. Zhang, J. Catal., 2010, 276, 16–23.
- 41 Z. Lendzion-Bielun, M. M. Bettahar and S. Monteverdi, Catal. Commun., 2010, 11, 1137–1142.
- 42 Tana, M. Zhang, J. Li, H. Li, Y. Li and W. Shen, *Catal. Today*, 2009, **148**, 179–183.
- 43 S. Watanabe, X. Ma and C. Song, J. Phys. Chem. C, 2009, 113, 14249–14257.
- 44 Z. Wu, M. Li, J. Howe, H. M. Meyer, 3rd and S. H. Overbury, *Langmuir*, 2010, **26**, 16595–16606.
- 45 H.-X. Fan, J. Feng and W.-Y. Li, Appl. Surf. Sci., 2019, 486, 411–419.
- 46 C. Beasley, M. K. Gnanamani, H. H. Hamdeh, M. Martinelli and B. H. Davis, *Catal. Lett.*, 2018, 148, 1920–1928.
- 47 B. M. Weckhuysen, I. E. Wachs and R. A. Schoonheydt, Chem. Rev., 1996, 96, 3327–3349.
- 48 X. Li, S. Wei, Z. Zhang, Y. Zhang, Z. Wang, Q. Su and X. Gao, *Catal. Today*, 2011, 175, 112–116.
- 49 K. Bian, G. Zhang, J. Zhu, X. Wang, M. Wang, F. Lou, Y. Liu, C. Song and X. Guo, ACS Catal., 2022, 12, 6559–6569.
- 50 Y. Ren, F. Zhang, W. Hua, Y. Yue and Z. Gao, *Catal. Today*, 2009, 148, 316–322.
- 51 E. Gomez, S. Kattel, B. Yan, S. Yao, P. Liu and J. G. Chen, Nat. Commun., 2018, 9, 1398.
- 52 T. D. Nguyen, W. Zheng, F. E. Celik and G. Tsilomelekis, Catal. Sci. Technol., 2021, 11, 5791–5801.
- 53 T. Shishido, K. Shimamura, K. Teramura and T. Tanaka, Catal. Today, 2012, 185, 151–156.
- 54 A. Hezam, K. Namratha, Q. A. Drmosh, D. Ponnamma, J. Wang, S. Prasad, M. Ahamed, C. Cheng and K. Byrappa, ACS Appl. Nano Mater., 2019, 3, 138–148.

- 55 E. Nowicka, C. Reece, S. M. Althahban, K. M. H. Mohammed, S. A. Kondrat, D. J. Morgan, Q. He, D. J. Willock, S. Golunski, C. J. Kiely and G. J. Hutchings, ACS Catal., 2018, 8, 3454-3468.
- 56 A. Siahvashi and A. A. Adesina, Ind. Eng. Chem. Res., 2013, 52, 15377-15386.
- 57 S. Chen, J. Zaffran and B. Yang, Appl. Catal., B, 2020, 270, 118859.
- 58 A. Hook, T. P. Nuber and F. E. Celik, Ind. Eng. Chem. Res., 2018, 57, 8131-8143.
- 59 M. Jørgensen and H. Grönbeck, ACS Catal., 2016, 6, 6730-6738.
- 60 M. Van den Bossche and H. Gronbeck, J. Am. Chem. Soc., 2015, 137, 12035-12044.
- 61 X. Zhang, X. Zhu, L. Lin, S. Yao, M. Zhang, X. Liu, X. Wang, Y.-W. Li, C. Shi and D. Ma, ACS Catal., 2016, 7, 912-918.
- 62 A. Hook and F. E. Celik, Ind. Eng. Chem. Res., 2018, 57, 6830-6841.
- 63 L. Huang, B. Han, Q. Zhang, M. Fan and H. Cheng, J. Phys. Chem. C, 2015, 119, 28934-28945.
- 64 M. Zhu and I. E. Wachs, ACS Catal., 2016, 6, 2827-2830.
- 65 X. Su, X. Yang, B. Zhao and Y. Huang, J. Energy Chem., 2017, 26, 854-867.

- 66 H. Xiong, S. Lin, J. Goetze, P. Pletcher, H. Guo, L. Kovarik, K. Artyushkova, B. M. Weckhuysen and A. K. Datye, Angew. Chem., Int. Ed., 2017, 56, 8986-8991.
- 67 E. Gomez, Z. Xie and J. G. Chen, AIChE J., 2019, 65, e16670.
- 68 J. Gascón, C. Téllez, J. Herguido and M. Menéndez, Appl. Catal., A, 2003, 248, 105-116.
- 69 F. M. Althenayan, S. Yei Foo, E. M. Kennedy, B. Z. Dlugogorski and A. A. Adesina, Chem. Eng. Sci., 2010, 65, 66-73.
- 70 R. You, X. Zhang, L. Luo, Y. Pan, H. Pan, J. Yang, L. Wu, X. Zheng, Y. Jin and W. Huang, J. Catal., 2017, 348, 189-199.
- 71 M. F. Delley, M.-C. Silaghi, F. Nuñez-Zarur, K. V. Kovtunov, O. G. Salnikov, D. P. Estes, I. V. Koptyug, A. Comas-Vives and C. Copéret, Organometallics, 2016, 36, 234-244.
- 72 A. Olafsen, A. Slagtern, I. Dahl, U. Olsbye, Y. Schuurman and C. Mirodatos, J. Catal., 2005, 229, 163-175.
- 73 P. Michorczyk, J. Ogonowski and K. Zeńczak, J. Mol. Catal. A: Chem., 2011, 349, 1-12.
- 74 P. Michorczyk, J. Ogonowski and M. Niemczyk, Appl. Catal., A, 2010, 374, 142-149.
- 75 M. Santhoshkumar, N. Hammer, M. Ronning, A. Holmen, D. Chen, J. Walmsley and G. Oye, J. Catal., 2009, 261, 116-128.
- 76 M. Huš, D. Kopač and B. Likozar, J. Catal., 2020, 386, 126-138.